

# C2H-

Benjamin A. Laws,<sup>\*,†,‡</sup> Zachariah D. Levey,<sup>†</sup> Timothy W. Schmidt,<sup>†</sup> and

Stephen T. Gibson<sup>‡</sup>

<sup>†</sup>*School of Chemistry, University of New South Wales, Sydney NSW 2052, Australia*

<sup>‡</sup>*Research School of Physics, The Australian National University, Canberra ACT 2601,  
Australia*

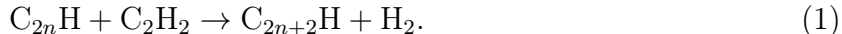
E-mail: b.laws@unsw.edu.au

## Abstract

## Introduction

Carbon monohydrides  $C_{2n}H$ , are a class of linear radicals that play an important role in combustion and interstellar chemistry. These carbon chains have been observed in many interstellar environments, including planetary atmospheres, comets, dark clouds, and during heavy star formation. Due to their relatively high abundance in a variety of astronomical conditions, they have been proposed to be promising candidates for Diffuse Interstellar Band carriers. The corresponding anions  $C_{2n}H^-$  are also believed to play an important role in interstellar chemistry.  $C_6H^-$  was the first negative ion detected in space, after it was observed in the circumstellar envelope of IRC+10216 in 2006. More recently, anions  $C_4H^-$  and  $C_8H^-$  have also been detected in a range of environments, include dark clouds, prestellar cores, and protellar envelopes.

Chain growth of the  $C_{2n}H$  radicals occurs predominately through acetylene addition,



Conversely, the formation of anions in space is believed to be driven by radiative electron attachment, charge transfer, and dissociate electron attachment. However modelling these processes underestimates the abundance of  $C_4H^-$  observed in IRC+10216. Therefore, ion-neutral reactions have been proposed as an additional chain growth mechanism that also needs to be considered,



Modelling of the extraterrestrial planetary atmosphere of Saturn's moon Titan, suggests that both  $C_2H$  and  $C_2H^-$  play an important role in the atmospheric chemistry. Multiple reaction

pathways were included for the ion  $\text{C}_2\text{H}^-$  including,



Understanding interstellar chemistry relies critically on theory, to provide a link between astronomical observations and terrestrial laboratory studies. Microwave spectroscopy has successfully been used in this fashion to identify a large number of molecules in the ISM. However for some species, particularly those with low abundances, UV/vis spectroscopic methods are required for identification. This creates a challenge for theory, as electronic spectra calculations are a lot more sensitive to the level of theory employed than pure rotational spectra. This becomes even more challenging when vibronic coupling effects are introduced, as they can be exceedingly difficult to model.

These considerations may be explored by examining some of the smallest carbon monohydrides. The ethynyl radical  $\text{C}_2\text{H}$  may appear to be a simple linear triatomic molecule. However the electronic spectrum is complicated by the presence of the close-lying ground  $^2\Sigma^+$  and first excited  $^2\Pi$  surfaces, which are only separated by  $\sim 4,000 \text{ cm}^{-1}$ . The interaction of these surfaces produces a complex vibronic spectrum around the  $\tilde{A}^2\Pi$  origin, where no single band corresponding to the  $\tilde{X} - \tilde{A}$  origin has been observed. In  $\text{C}_4\text{H}$  the  $^2\Sigma^+$  and  $^2\Pi$  states are nearly degenerate, resulting in even stronger coupling, while in  $\text{C}_6\text{H}$  and  $\text{C}_8\text{H}$  the ordering of the states swaps, with a ground  $^2\Pi$  state and a low lying excited  $^2\Sigma^+$  state. Consequently, understanding these vibronic coupling interactions between the  $^2\Sigma$  and  $^2\Pi$  surfaces will be essential in order to accurately model the role these radicals (and their corresponding anions) are likely to play in the interstellar chemistry mentioned above, and to discern if they may be possible DIB carriers.

In this paper we study the vibronic spectrum of the ethynyl radical  $\text{C}_2\text{H}$  by employing High-Resolution Photoelectron Imaging (HR-PEI) in order to benchmark CFOUR *ab-initio* vibronic-coupling calculations.  $\text{C}_2\text{H}$  is reported to be one of the most abundant molecules in the universe, and is the most thoroughly studied of the  $\text{C}_{2n}\text{H}$  species. Many different experimental techniques have been employed to try and resolve the complex vibronic spectrum, including electron spin resonance, laser magnetic resonance, microwave and milli-meter wave spectroscopy, infrared (matrix isolation and Fourier Transform) spectroscopy, and photoelectron spectroscopy. Extensive theoretical work on  $\text{C}_2\text{H}$  has also been carried out, in order to try and decode the surprisingly complex spectra that are observed in the experimental studies, however this has proven to be far from straightforward. In this work we demonstrate how the procedures set out in CFOUR may be used to calculate the strength of the vibronic interaction between coupled surfaces near a conical intersection, in order to simulate electronic and vibronic spectra. By employing anion HR-PEI both the  $^2\Sigma^+$  and  $^2\Pi$  surfaces are mapped out on an equal footing from the anion  $\tilde{X}^1\Sigma^+$  state, allowing for direct comparison to the *ab-initio* modelling.

## Results and Analysis

Ethynyl ions were produced in a pulsed-jet discharge of pure  $\text{C}_2\text{H}_4$  gas, and subsequently mass isolated via time of flight. Electrons were detached using a tuneable Sunlite Optical Parametric Oscillator (OPO) pumped with the third harmonic of a Nd:YAG laser. High electron counts could also be obtained by using the third and fourth harmonics of the Nd:YAG laser directly. The detached electrons were then mapped onto a micro channel plate detector using a Velocity Map Imaging (VMI) lens. An illustrative VMI of  $\sim 4$  million electrons collected from 355 nm (3.49 eV) photodetachment of  $\text{C}_2\text{H}^-$  is shown in Fig. 1(a). The electrons are distributed radially according to their speed, with slow electrons at the image center, and fast electrons located towards the outer edge. Due to the relatively large  $\text{C}_2\text{H}^-$  elec-

tron affinity (EA) of 2.969 eV,<sup>1</sup> photodetachment at 355 nm occurs close to threshold. This yields slow electrons, allowing for a low repeller voltage (−600 V) on the VMI lens, and high velocity resolution.

Despite being close to threshold, two electronic states of neutral C<sub>2</sub>H are observed. The faster electrons on the outer edge correspond to C<sub>2</sub>H( $\tilde{X}^2\Sigma^+$ ) + e<sup>−</sup> ← C<sub>2</sub>H<sup>−</sup>( $\tilde{X}^1\Sigma^+$ ) + hν photodetachment, and are preferentially distributed around the poles of the image, indicative of a positive anisotropy parameter. Conversely the angular distribution of the slower electrons near the center are skewed towards the equator, indicative of a negative anisotropy parameter. These electrons may be assigned to photodetachment to the first excited state C<sub>2</sub>H( $\tilde{A}^2\Pi$ ) + e<sup>−</sup> ← C<sub>2</sub>H<sup>−</sup>( $\tilde{X}^1\Sigma^+$ ) + hν.

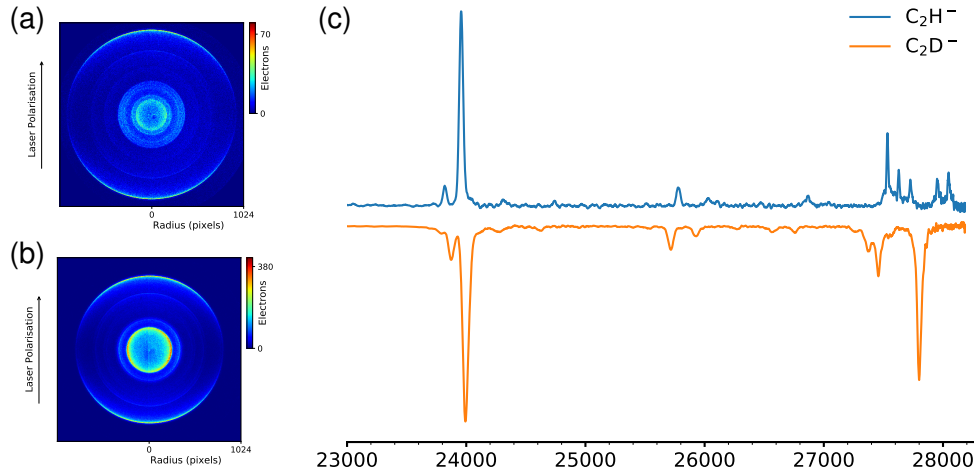


Figure 1: (a) A 3D-representation of the velocity-map image of  $\sim 4$  million photoelectrons detached from C<sub>2</sub>H<sup>−</sup> at 355 nm. The outer rings, distributed around the vertical laser polarisation axis, represents photodetachment to the ground  $\tilde{X}^2\Sigma^+$  state. The inner rings represent detachment to the first excited state  $\tilde{A}^2\Pi$ . (b) Photoelectron spectra of C<sub>2</sub>H<sup>−</sup> at a range of detachment wavelengths, illustrating the change in electron intensity profile and energy resolution.

To investigate the vibronic coupling interaction between these two nearby  $\Sigma^+$  and  $\Pi$  surfaces, deuterated ethynyl C<sub>2</sub>D<sup>−</sup> was also studied. C<sub>2</sub>D<sup>−</sup> ions were produced in a discharge of pure C<sub>2</sub>D<sub>4</sub> gas and measured under the same experimental conditions as C<sub>2</sub>H<sup>−</sup>. An illustrative VMI of photodetachment at 355 nm from C<sub>2</sub>D<sup>−</sup> is shown in Fig. 1(b). Similarly to

Fig 1(a) two electronic states are observed - fast electrons with a positive anisotropy corresponding to detachment to the  $^2\Sigma^+$  surface, and slow electrons with a negative anisotropy corresponding to  $^2\Pi$  detachment. While the fast electrons appear similar in both images, a striking difference is observed in the slow electrons near the detector center. In Fig. 1(a) a series of weak rings are observed, however in Fig. 1(b) two dominant rings are seen.

The VMI in Fig. 1 were inverted using the Abel inversion methods detailed in pyAbel, to extract the corresponding photoelectron spectra, which are presented in Fig. 1(c). Below 27,000  $\text{cm}^{-1}$  the  $\text{C}_2\text{H}^-$  and  $\text{C}_2\text{D}^-$  spectra appear very similar. Both are dominated by the origin transition, shifted by  $\sim 10 \text{ cm}^{-1}$  in the deuterated spectrum, and show a progression in the  $2_0^{n+1}$  and  $3_0^1 2_0^{n+1}$  vibrational modes. Within the harmonic oscillator approximation, transitions involving an odd quanta of vibrational excitation in the non-symmetric  $v_2(\pi)$  mode should be totally forbidden. However, their presence in the photoelectron spectrum in Fig. 1(c) is likely an indicator of Herzberg-Teller (HT) vibronic coupling between the ground  $^2\Sigma^+$  and nearby excited  $^2\Pi$  electronic surfaces, as

$$\Sigma^+ \otimes \pi = \Pi. \quad (7)$$

Above 27,000  $\text{cm}^{-1}$ , near the  $\tilde{A}^2\Pi$  state origin, large differences are observed between the  $\text{C}_2\text{H}^-$  and  $\text{C}_2\text{D}^-$  photoelectron spectra in Fig. 1(c). In the  $\text{C}_2\text{H}^-$  spectrum 5 sharp peaks are observed, spaced by  $\sim 95 \text{ cm}^{-1}$ . However in the deuterated spectrum, one dominant peak is observed at 27,792  $\text{cm}^{-1}$ , with 3 weaker peaks centred around 27,360  $\text{cm}^{-1}$ . Unlike the structure below 27,000  $\text{cm}^{-1}$  none of these peaks are able to be readily assigned to vibronic transitions, due to the presence of strong coupling interactions between the nearby  $\Sigma^+$  and  $\Pi$  surfaces.

## Vibronic Coupling Interactions

The surprisingly complex spectral structure observed near the  $\tilde{A}^2\Pi$  state origin in the photoelectron spectra in Fig. 1(c), may be understood by considering the  $v_2$  bending vibrational mode. To account for the degeneracy of this mode we may introduce the vibronic quantum number  $\ell_i$ , representing the angular momentum associated with the bending motion. This may take a value of  $\ell_i = v_i, v_i - 2, v_i - 4, \dots, 1$  or  $0$ , where  $v_i$  is the quanta of bending excitation. In the Born-Oppenheimer approximation different vibronic energy levels  $\ell_i$  are degenerate, however in cases with strong rovibronic coupling, this degeneracy in  $\ell_i$  is lost.

In  $C_2H$  this effect creates a Renner-Teller (RT) pair in the excited state, where the usually degenerate  $\Pi$  surfaces separate to form two non-degenerate electronic states  $\Pi^+(2A')$  and  $\Pi^-(1A'')$ . This involves separating a single potential energy surface (V) into two distinct but connected surfaces ( $V^+$ ) and ( $V^-$ ). Due to the strong coupling along the linear axis between the electronic and vibration angular momenta of the  $2A'$  and  $1A''$  components of the  $^2\Pi$  state, stationary states cannot be explicitly assigned to either of the  $\Pi^+(2A')$  or  $\Pi^-(1A'')$  electronic surfaces. Instead, they exist as a combination of both states.

Due to the close lying nature of the ground  $\tilde{X}^2\Sigma^+$  and excited  $\tilde{A}^2\Pi$  electronic states, which are only separated by  $\sim 3700 \text{ cm}^{-1}$ , a pseudo Jahn-Teller effect is also observed. The Jahn-Teller theorem states that stability and degeneracy are not possible simultaneously unless the molecule is linear,<sup>2</sup> meaning that non-linear molecules with degenerate electronic states will undergo a symmetry breaking distortion in order to remove the degeneracy. However a similar effect has also been observed where coupling exists between a non-degenerate state and a nearby pair of degenerate states, even if a molecule is linear.

In the case of ethynyl this is seen as coupling between the ground  $\Sigma^+(1A')$  and excited  $\Pi^+(2A')$  states, induced by the bending motion of  $v_2$ . The ground state only couples to one of the Renner-Teller pair  $\Pi^+(2A')$ , as the other state  $\Pi^-(1A'')$  has incorrect symmetry. This results in a very complex vibronic structure for the  $\tilde{A}^2\Pi$  electronic state, with contributions from three coupled surfaces  $\Sigma^+(1A')$ ,  $\Pi^+(2A')$ , and  $\Pi^-(1A'')$ .

These interactions spread the electronic origin of the  $\tilde{A}^2\Pi$  state over several vibronic levels. Therefore, instead of assigning a defined origin, the observed peaks in the spectrum may be assigned to coupled admixtures of vibronic transitions involving the three potential energy surfaces,

$$\Psi_f = \sum_{\xi} \psi_e^{\xi} \sum_k C_{fk}^{\xi} \phi_{fkm}^{\xi}, \quad (8)$$

where  $\psi_e^{\xi}$  is the diabatic electronic wavefunction, and  $\phi_{fkm}^{\xi}$  is the spin-rovibrational wavefunction.  $\xi$  represents the electronic states used in the expansion, and in this case  $\xi = \Sigma^+(1A')$ ,  $\Pi^+(2A')$ ,  $\Pi^-(1A'')$ . A depiction of these three interacting surfaces is given in Fig. 2.

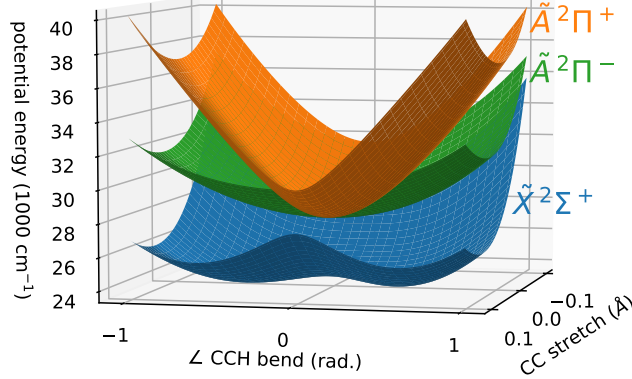


Figure 2: Adiabatic potential energy surfaces of  $\tilde{X}^2\Sigma^+$ ,  $\tilde{A}^2\Pi^-$ , and  $\tilde{A}^2\Pi^+$  states, calculated using the method developed by Tarroni and Carter<sup>?</sup> ( $E_{1A'}$ ,  $E_{2A'}$ , and  $E_{1A''}$  in Eq. 8).

Tarroni and Carter<sup>?</sup> have demonstrated that a large number of admixed vibronic levels may be calculated using the potential energy surfaces in Fig. 2. In fact, over 100 vibronic levels have been calculated, up to  $6,400 \text{ cm}^{-1}$  above the  $\tilde{X}$  state origin. However assigning these levels to experimental spectra has remained a challenge, partly due to the large number of calculated vibronic levels, and partly due to the resolution of the experimental data in the literature.



## Coupling Calculations

In order to guide spectral assignment of  $\text{C}_2\text{H}$  and astronomical searches for other  $\text{C}_n\text{H}$  radicals, transition intensities are also needed. However, due to the strong vibronic coupling interactions, this can not be obtained via standard quantum chemistry methods. To account for these interactions, the photoelectron spectrum of the  $\text{C}_2\text{H}^-$  anion was simulated using a quasidiabatic Hamiltonian of the type advocated by Koeppel, Domcke and Cederbaum (KDC, reference here). In this approach, the Hamiltonian is represented in a basis of quasidiabatic (slowly varying) electronic states for which the kinetic energy operator can be assumed diagonal. For  $\text{C}_2\text{H}$ , the KDC Hamiltonian comprises three states - the two components of the  $^2\Pi$  state and the ground  $^2\Sigma$  state - and is then projected onto a vibrational basis, usually chosen as a direct product of harmonic oscillators. Diagonalization of the corresponding matrix yields the molecular states (which are given in terms of a Born-Huang expansion), and the squared projections of the corresponding eigenvectors onto the ground state of the anion yield the relative intensities. The latter is automatically true if the photodetachment cross sections for the  $^2\Sigma$  and  $^2\Pi$  states are assumed equal, but different cross sections of the two states can be incorporated by scaling the intensities of states according to their (vibronic) symmetry.

Details of the construction and parametrization of KDC Hamiltonians can be found elsewhere in the literature (references), and the procedure followed will be discussed here only briefly. The present calculations use the so-called quadratic vibronic coupling (QVC) model. For the system at hand, the QVC model Hamiltonian assumes the following form

where the summations run over the dimensionless normal modes ( $q_i$ ) that serve as the coordinate system for the problem. For convenience, the latter are chosen to be those of the anion, which considerably facilitates calculation of the spectral intensities. In Eq. 1, the diagonal terms of  $V$  (excluding those that carry the Renner-Teller coupling constant  $\eta$ ) represent the quasidiabatic potential energy surfaces of the  $\Sigma$ , and the two components of the  $\Pi$  state, chosen here as those in which the unpaired electron lies within or is perpen-

dicular to an arbitrarily chosen plane, designated as A(a') and A(a''), respectively.  $\Delta_0^X$  is the separation of the anion and  $\Sigma$  states at the origin of the coordinate system (the vertical electron detachment energy), and  $\Delta_0^{Pi}$  is the gap between anion and  $\Pi$  states at the same geometry.

For the modes of  $\sigma$  symmetry ( $q_1$  and  $q_3$ ), the diabatic forces ( $F_i$ ) and force constants ( $F_{ij}$ ) coincide with those of the adiabatic potential energy surfaces. However, for the bending mode, the diabatic (F22) and adiabatic (f22) force constants differ, and the parametrization is somewhat more involved. For each component of the  $\Pi$  state, either the 2a or 2b component of the bending vibration will maintain the A' electronic symmetry that is needed to couple with the X state. Designating these as 2a for the A(a') state and 2b for the A(a'') state (as is implicit in Eq. 1), the diabatic force constants for the bending mode in the X and A states can be written as

where the Renner-Teller interaction strength ( $\eta$ ) is determined from

once the interstate coupling ( $\lambda$  which is calculated analytically in this work, see below) is known.

When the potential in Eq. 1 is diagonalized, the adiabatic states that are used for its parametrization are precisely recovered through second order in displacement. To parametrize this Hamiltonian, the equation-of-motion coupled-cluster method known as EOMIP-CCSDT has been used ... (Zach goes from here)...

$$V = \begin{matrix} & \begin{matrix} X & A(a') & A(a'') \end{matrix} \\ \begin{matrix} X \\ A(a') \\ A(a'') \end{matrix} & \left( \begin{array}{ccc} \Delta_0^X + F_1^X q_1 + F_3^X q_3 + \frac{1}{2} \sum_{ij} F_{ij}^X q_i q_j & 0 & 0 \\ 1 & \Delta_0^A + F_1^A q_1 + F_3^A q_3 + \frac{1}{2} \sum_{ij} F_{ij}^A q_i q_j + \frac{1}{2} \eta (q_{3a}^2 - q_{3b}^2) & 0 \\ 0 & 1 & 0 \end{array} \right) \end{matrix} \quad (9)$$

## Simulated Spectra

The above method was employed to simulate the photoelectron spectrum of  $\text{C}_2\text{H}^-$ , with the calculated transitions compared to the experimental data in Figure a. The positions of the  $^2\Pi$  levels have been shifted by  $1,220\text{ cm}^{-1}$  to account for the EOMIP-CCSDT calculations overestimating the effective  $^2\Pi$  Term energy. Excellent agreement is seen below the A state origin ( $\text{xxx cm}^{-1}$ ) in both the position and intensity of the calculated transitions. This includes the Herzberg-Teller coupled transitions, with  $\Pi$  symmetry.

The calculations also show good agreement near the conical intersection, correctly predicting that the A state origin is spread over 5 prominent transitions. The relative calculated intensities are also a good match to the experimental data. Peak e may appear overestimated in the calculations, however this may be explained by the Wigner threshold law reducing the intensity of the experimental peak as it is close to threshold at 355nm. The simulated spectrum slightly underestimates the splitting between the vibronic levels, however this may be linked to the overestimation of the gap between the  $^2\Sigma$  and  $^2\Pi$  surfaces.

The deuterated spectrum of  $\text{C}_2\text{D}^-$  was also simulated using the same approach, and is shown in Figure b. Again, there is excellent agreement in the intensity and calculated positions of the transitions on the X state surface. Near the A state origin, 3 strong transitions are calculated, which may be assigned to the 3 dominant peaks in the experimental spectrum (a,b,c). Two transitions are calculated at the position of peak a, however due to the small spacing this may not be resolved in the experimental data. The calculated transition for peak c appears to slightly underestimate both the intensity and splitting compared to the experimental data.

The calculated transitions were used to simulate the photoelectron spectrum at 266 nm, as shown in Figure c. Gaussians were fitted to the transitions with a FWHM of  $20\text{ cm}^{-1}$  to match the resolution of the experimental data. This figure demonstrates that the method used in this work does in excellent job in qualitatively predicting the photoelectron spectrum of molecules involving complex vibronic coupling interactions. This result also confirms that

the method is able to calculate the intensity and position of levels higher up the coupled A state surface. Near the  $3^0$  transitions ( $5,000\text{ cm}^{-1}$ ) only peak f appears to be missing from the simulated spectrum.

Overall, figures a-c show that the quasiadiabatic approach is a reliable method for simulating the spectra of molecules when strong vibronic coupling interactions are involved. This method may be expanded to other  $C_nH$  radicals that possess similar complexities, in order to help guide the search for new molecules to be found in space.

## Photoelectron Angular Distributions

Symmetry considerations may be employed to help verify the assignments from the calculations above. The EOMIP-CCSDT calculations determine the symmetry of each transitions, either  $\Sigma$  or  $\Pi$ . Experimentally, this may be compared directly to symmetries obtained from the corresponding photoelectron angular distributions. As the detachment laser is linearly polarized, the angular distribution of the electrons in Fig. 1 may be linked to the symmetry of the detachment orbital. For polarised light, the differential cross section is given by

$$\frac{d\sigma}{d\Omega} = \frac{\sigma_{\text{total}}}{4\pi} [1 + \beta P_2(\cos \theta)], \quad (10)$$

where  $\theta$  is the angle between the ejected electron and the (vertical) laser polarization, and  $P_2$  is the second-order Legendre polynomial. The anisotropy parameter  $\beta$  provides a quantitative measure of the angular distribution, and can range from -1 to +2 for a pure parallel and perpendicular transition respectively.\*\* From Eq. (12),  $\beta$  may be determined for each transition in a photoelectron spectrum from the slope of  $I(\theta)$  vs  $P_2(\cos \theta)$ .

Through conservation of angular momentum, it can be shown that  $\beta$  may also be expressed in terms of partial waves and dipole matrix elements. Explicitly,

$$\beta_\ell = \frac{[\ell(\ell-1)\chi_{\ell,\ell-1}^2 + (\ell+1)(\ell+2)\chi_{\ell,\ell+1}^2 - 6\ell(\ell+1)\chi_{\ell,\ell-1}\chi_{\ell,\ell+1}\cos\delta_{\ell+1,\ell-1}]/(2\ell+1)}{\ell\chi_{\ell,\ell-1}^2 + (\ell+1)\chi_{\ell,\ell+1}^2}, \quad (11)$$

where  $\ell$  is the electron orbital angular momentum of the parent anion orbital,  $\chi_{\ell,\ell\pm 1}$  is the radial dipole matrix element for the transition from an orbital  $\ell$  to each of the  $\ell \pm 1$  partial waves, and  $\delta_{\ell+1,\ell-1}$  is the phase shift between the two ( $\ell \pm 1$ ) partial waves.

Photodetachment to the ground state of  $\text{C}_2\text{H}^-$  ( $\tilde{X}^1\Sigma^+$ ) involves ejecting an electron from an  $s$ -like  $5\sigma_g$  orbital, whereas detachment to the excited ( $\tilde{A}^2\Pi$ ) state occurs from a  $p$ -like  $1\pi_u$  orbital.

Symmetry considerations can be employed to help assign the admixed structure in the experimental photoelectron spectra around the  $\tilde{A}^2\Pi$  origin. As the detachment laser is linearly polarized, the angular distribution of the electrons in Fig. 1 may be linked to the symmetry of the detachment orbital. For polarised light, the differential cross section is given by

$$\frac{d\sigma}{d\Omega} = \frac{\sigma_{\text{total}}}{4\pi} [1 + \beta P_2(\cos \theta)], \quad (12)$$

where  $\theta$  is the angle between the ejected electron and the (vertical) laser polarization, and  $P_2$  is the second-order Legendre polynomial. The anisotropy parameter  $\beta$  provides a quantitative measure of the angular distribution, and can range from -1 to +2 for a pure parallel and perpendicular transition respectively.\*\* From Eq. (12),  $\beta$  may be determined for each transition in a photoelectron spectrum from the slope of  $I(\theta)$  vs  $P_2(\cos \theta)$ . Through conservation of angular momentum, it can be shown that  $\beta$  may also be expressed in terms of partial waves and dipole matrix elements. Explicitly,

$$\beta_\ell = \frac{[\ell(\ell-1)\chi_{\ell,\ell-1}^2 + (\ell+1)(\ell+2)\chi_{\ell,\ell+1}^2 - 6\ell(\ell+1)\chi_{\ell,\ell-1}\chi_{\ell,\ell+1}\cos\delta_{\ell+1,\ell-1}]/(2\ell+1)}{\ell\chi_{\ell,\ell-1}^2 + (\ell+1)\chi_{\ell,\ell+1}^2}, \quad (13)$$

where  $\ell$  is the electron orbital angular momentum of the parent anion orbital,  $\chi_{\ell,\ell\pm 1}$  is the radial dipole matrix element for the transition from an orbital  $\ell$  to each of the  $\ell \pm 1$  partial waves, and  $\delta_{\ell+1,\ell-1}$  is the phase shift between the two ( $\ell \pm 1$ ) partial waves.

As the radial dipole matrix elements will vary with electron kinetic energy, so too will  $\beta$ . Therefore, measuring anisotropy parameters at a range of energies will reveal the character

of the detachment orbital. Anisotropy parameters were calculated for all resolved transitions in the  $\text{C}_2\text{H}^-$  photoelectron spectra from 266 – 355 nm, as shown in Fig. ??.

Photodetachment to the ground state of  $\text{C}_2\text{H}^-$  ( $\tilde{X}^1\Sigma^+$ ) involves ejecting an electron from an  $s$ -like  $5\sigma_g$  orbital, whereas detachment to the excited ( $\tilde{A}^2\Pi$ ) state occurs from a  $p$ -like  $1\pi_u$  orbital. For a pure  $s$  and  $p$  orbital, the energy dependence of the anisotropy parameter may be described by Equations (14) and (15) respectively,

$$\beta_s = 2, \quad (14)$$

and,

$$\beta_p = \frac{2A_1^2\epsilon^2 - 4A_1\epsilon \cos \delta_{2,0}}{1 + 2A_1^2\epsilon^2}, \quad (15)$$

where the Hanstorp coefficient  $A_1$  relates to the ratio of radial matrix elements  $\frac{\chi_{1,2}}{\chi_{1,0}}$  and  $\delta_{2,0}$  represents the partial wave phase shift. As molecular orbitals may not be pure, we can describe the detachment from  $\text{C}_2\text{H}^-$  using the mixed  $sp$  model of Sanov,<sup>3</sup>

$$\beta(\epsilon)_{sp} = \frac{2Z\epsilon + 2A_1\epsilon^2 - 4\epsilon \cos \delta_{\ell\pm 1}}{\frac{1}{A_1} + 2A_1\epsilon^2 + Z\epsilon} \quad (16)$$

where  $f$  is the percentage of  $p$  character of the orbital,

$$Z = \frac{1-f}{f} \frac{8}{3} \quad \text{and} \quad |\psi\rangle = \sqrt{1-f}|s\rangle + \sqrt{f}|p\rangle. \quad (17)$$

Therefore, calculating the anisotropy parameter for a given transition will reveal the symmetry of the state, which can be compared to the symmetry of the calculated vibronic levels. However this is complicated by the presence of HT coupling, which allows for the electronic character of two surfaces to be mixed via a vibrational promoting mode. As shown in the Supplementary Materials, the transition dipole moment for a HT coupled transition

may be rewritten as

$$\mu_{\alpha}^{a-n} = \langle \Psi_{\text{anion}} | \vec{\mu}_{\alpha} | \Psi_{\text{neutral}} \rangle \quad (18)$$

$$= \mu_{\alpha:0}^{\tilde{X}-\tilde{X}} \langle \chi''_{ms} | \chi'_{jt} \rangle + \gamma_{kr,jt} \mu_{a:0}^{\tilde{A}-\tilde{X}} \langle \chi''_{ms} | Q_n | \chi'_{kr} \rangle \quad (19)$$

where  $\mu_{\alpha:0}^{\tilde{X}-\tilde{X}}$  and  $\mu_{a:0}^{\tilde{A}-\tilde{X}}$  are the electronic transition moments for the  $\tilde{X} \leftarrow \tilde{X}$  and  $\tilde{A} \leftarrow \tilde{X}$  transitions,  $\chi''_{ms}$ ,  $\chi'_{jt}$ , and  $\chi'_{kr}$  are the nuclear components of the anion and neutral respectively, and  $\gamma_{kr,jt}$  is the vibronic coupling constant. Therefore, HT coupled transitions on the  $\tilde{X}^2\Sigma^+$  surface are expected to have anisotropy parameters that reflect the coupled  $\tilde{A}^2\Pi$  surface.

Anisotropy parameters were calculated for all strong transitions in the  $\text{C}_2\text{H}^-$  photoelectron spectra from 355 – 266 nm, as shown in Fig. ??.

HT coupling allows for the electronic character of two surfaces to be mixed via a vibrational promoting mode. As shown in the Supplementary Materials, the transition dipole moment for a HT coupled transition may be rewritten as

$$\mu_{\alpha}^{a-n} = \langle \Psi_{\text{anion}} | \vec{\mu}_{\alpha} | \Psi_{\text{neutral}} \rangle \quad (20)$$

$$= \mu_{\alpha:0}^{\tilde{X}-\tilde{X}} \langle \chi''_{ms} | \chi'_{jt} \rangle + \gamma_{kr,jt} \mu_{a:0}^{\tilde{A}-\tilde{X}} \langle \chi''_{ms} | Q_n | \chi'_{kr} \rangle \quad (21)$$

where  $\mu_{\alpha:0}^{\tilde{X}-\tilde{X}}$  and  $\mu_{a:0}^{\tilde{A}-\tilde{X}}$  are the electronic transition moments for the  $\tilde{X} \leftarrow \tilde{X}$  and  $\tilde{A} \leftarrow \tilde{X}$  transitions,  $\chi''_{ms}$ ,  $\chi'_{jt}$ , and  $\chi'_{kr}$  are the nuclear components of the anion and neutral respectively, and  $\gamma_{kr,jt}$  is the vibronic coupling constant. By comparing Eq. (21) to a Taylor series expansion of the transition dipole moment in  $Q_n$  about the anion equilibrium geometry, one can see that the vibronic coupling constant may be defined as,

$$\left( \frac{\partial \mu_{\alpha}^{\tilde{X}-\tilde{X}}}{\partial Q_n} \right)_0 = \gamma_{kr,jt} \mu_{a:0}^{\tilde{A}-\tilde{X}}. \quad (22)$$

Equation (22) shows that information about the vibronic coupling interaction between the

neutral  $\tilde{A} - \tilde{X}$  states may be obtained from determining the slope of the  $\tilde{X} - \tilde{X}$  electronic transition moment along the vibrational promoting mode coordinate  $Q_n$ .

The resolution attainable using velocity-map imaging is dependent on the energy of the photoelectrons,  $\Delta\epsilon \propto \epsilon$ . Therefore, measurements close to threshold will provide the highest energy resolution, while shorter wavelength measurements will map a greater extent of the neutral vibrational structure. This variation is illustrated in Fig. 1(b), which shows the photoelectron spectra of  $\text{C}_2\text{H}^-$  resulting from photodetachment at 266 nm, 300 nm, 310 nm, 320 nm, and 355 nm. In the shorter wavelength measurements, spectral structure related to the  $\tilde{A}^2\Pi$  state is observed up to  $6000\text{ cm}^{-1}$  above the  $\tilde{A}$  state origin. A high resolution photoelectron spectrum of  $\text{C}_2\text{H}^-$  detachment at 355 nm extracted from a  $2048 \times 2048$  image, similar to Fig. 1(a), via an inverse Abel transformation, is shown in Fig. ??

# Conclusions

# Methods

Details of the HR-PEI spectrometer are given in Refs 4 and 5.  $\text{CH}_2\text{CN}^-$  ions are produced by passing a 1:1  $\text{C}_2\text{H}_4:\text{N}_2\text{O}$  gas mixture through a pulse valve, which then undergoes supersonic expansion into a high-voltage discharge. Negative ions are extracted, accelerated to 500 eV, and focussed into a novel gating, bunching, and re-referencing unit.<sup>6</sup> Anions are mass separated over a 2m time-of-flight region, with the ion of interest isolated by an electrostatic gate. The ion packet is crossed with a tuneable detachment laser beam, generated from a Sunlite EX optical parametric oscillator pumped by the third harmonic of a Continuum Powerlite 9010 Nd:YAG laser. The laser produces between 10-50mJ per pulse at 10Hz, depending on whether the idler or signal beam is used. The wavelength of the laser light is measured using a HighFinesse WS7 UV wavemeter.

A velocity-map imaging lens, a modified version of the original concept of Eppink and



Parker, images the detached electrons to a 75mm diameter MCP/phosphor screen detector. Events are imaged by a 2048x2048 monochrome CCD camera (PCO 2000), with each frame transferred to a computer at a 10Hz repetition rate, and processed in real time to identify individual electron events. The electron positions are centroided to a sub-pixel accuracy, then written to a data file for subsequent analysis. The velocity-map image is centred and then circularized by an angular dependent-radial scaling determined by comparing adjacent radial slice intensity profiles.<sup>7</sup> An inverse Abel transformation of the VMI, based on the algorithm of Hansen and Law,<sup>8,9</sup> returns a slice image of the 3D electron source distribution. Absolute energy calibration of the photoelectron spectra is achieved using published measurements of species, including  $O^{-4}$  and  $NO_2^{-}$ ,<sup>?</sup> that have been studied under similar conditions as used for the  $CH_2CN^{-}$  measurements.

In standard operation, the energy distribution of the detached electrons is obtained by recording the velocity-mapped positions from photodetachment at a fixed wavelength. However the HR-PEI spectrometer may also be reconfigured into an electron counting mode, where the number of events per laser shot is recorded, while the detachment laser wavelength is varied.

## Acknowledgement

This research was supported by the Australian Research Council Discovery Project Grants DP160102585 and DP190103151.

## References

- (1) Ervin, K. M.; Lineberger, W. C. Photoelectron spectra of dicarbon(1-) and ethynyl(1-). *The Journal of Physical Chemistry* **1991**, *95*, 1167–1177.
- (2) Jahn, H. A.; Teller, E. Stability of polyatomic molecules in degenerate electronic states

- I Orbital degeneracy. *Proceedings of the Royal Society of London A: Mathematical, Physical and Engineering Sciences* **1937**, 161, 220–235.
- (3) Sanov, A. Laboratory-Frame Photoelectron Angular Distributions in Anion Photodetachment: Insight into Electronic Structure and Intermolecular Interactions. *Annual Review of Physical Chemistry* **2014**, 65, 341–363.
- (4) Cavanagh, S. J.; Gibson, S. T.; Gale, M. N.; Dedman, C. J.; Roberts, E. H.; Lewis, B. R. High resolution velocity-map imaging photoelectron spectroscopy of the  $O^-$  fine-structure transitions. *Physical Review A* **2007**, 76, 052708.
- (5) DeVine, J. A.; Weichman, M. L.; Laws, B.; Chang, J.; Babin, M. C.; Balerdi, G.; Xie, C.; Malbon, C. L.; Lineberger, W. C.; Yarkony, D. R. et al. Encoding of vinylidene isomerization in its anion photoelectron spectrum. *Science* **2017**, 358, 336–339.
- (6) Dedman, C. J.; Roberts, E. H.; Gibson, S. T.; Lewis, B. R. Fast 1 kV metal-oxide-semiconductor field-effect transistor switch. *Review of Scientific Instruments* **2001**, 72, 3718–3720.
- (7) Gascooke, J. R.; Gibson, S. T.; Lawrance, W. D. A “circularisation” method to repair deformations and determine the centre of velocity map images. *The Journal of Chemical Physics* **2017**, 147, 013924.
- (8) Hansen, E. W.; Law, P.-L. Recursive methods for computing the Abel transform and its inverse. *Journal of the Optical Society of America A* **1985**, 2, 510–520.
- (9) Hickstein, D. D.; Yurchak, R.; Das, D.; Shih, C.-Y.; Gibson, S. T. PyAbel (v0.7): A Python package for Abel transforms. <https://github.com/PyAbel/PyAbel>, 2016.